

# Wire-based sternal closure: MRI-related heating at 1.5 T/64 MHz and 3 T/128 MHz based on simulation and experimental phantom study

Jianfeng Zheng<sup>1</sup>  | Meiqi Xia<sup>1</sup> | Wolfgang Kainz<sup>2</sup> | Ji Chen<sup>1</sup> 

<sup>1</sup>Department of Electrical and Computer Engineering, University of Houston, Houston, Texas

<sup>2</sup>Division of Biomedical Physics, Office of Science and Engineering Laboratories, Center for Devices and Radiological Health, US Food and Drug Administration, Silver Spring, Maryland

## Correspondence

Ji Chen, Department of Electrical and Computer Engineering, University of Houston, 4800 Calhoun Blvd., Houston, TX 77004.

Email: jchen23@central.uh.edu

**Purpose:** The paper investigates factors that affect the RF-induced heating for commonly used wire-based sternal closure under 1.5 T and 3 T MRI systems and clarifies the heating mechanisms.

**Methods:** Numerical simulations based on the finite-difference time-domain method and experimental measurements in ASTM (American Society for Testing and Materials) phantom were used in the study. Various configurations of the wire-based sternal closure in the phantom were studied based on parameter sweeps to understand key factors related to the RF-induced heating. In vivo simulations were further performed to explore the RF-induced heating in computational human phantoms for clinically relevant scenarios.

**Results:** The wire-based sternal closure can lead to peak 1-g averaged spatial absorption ratio of 106.3 W/kg and 75.2 W/kg in phantom and peak 1-g averaged specific absorption rate of 32.1 W/kg and 62.1 W/kg in computational human models near the device at 1.5 T and 3 T, respectively. In phantom, the simulated maximum temperature rises for 15-minute RF exposure are 9.4°C at 1.5 T and 5.8°C at 3 T. Generally, the RF-induced heating will be higher when the electrical length of the device is close to the resonant length or when multiple components are spaced closely along the longitudinal direction.

**Conclusion:** The RF-induced heating related to wire-based sternal closure can be significant due to the antenna effect and capacitive mutual coupling effect related to the specific geometries of devices.

## KEYWORDS

antenna effect, capacitive mutual coupling effect, magnetic resonance imaging (MRI), RF-induced heating, wire-based sternal closure

## 1 | INTRODUCTION

Magnetic resonance imaging is one of the most effective, safe, and commonly used clinical imaging techniques for medical diagnosis and following-up treatments. It is especially suitable for soft tissue imaging and does not use harmful ionized radiations.<sup>1</sup> However, there are still safety concerns for patients with implantable devices during MRI procedure because of the safety risks caused by interactions between the implanted devices and magnetic/electromagnetic fields from the MRI equipment.<sup>2-5</sup> Various statements and guidelines have been proposed to manage the safety issues regarding MRI examinations in patients with implants.<sup>5-9</sup> In these, understanding the interactions between implants and MRI environments is the basis and key point. Among all of the safety concerns, the RF-induced heating is a major concern due to the complex relationships between the RF heating and MRI environments.<sup>10-12</sup> For implantable devices, especially those with metallic components, the RF-induced energy from MRI may lead to hot spots near the devices and generate a high temperature rise in the surrounding lossy human tissues.<sup>13-16</sup> This can lead to instant patient tissue damage.

To determine conditions under which the patients can be safely scanned, the RF-induced heating for the implants should be carefully and comprehensively evaluated. Once the safe conditions are determined, the appropriate MR condition can be labeled per ASTM (American Society for Testing and Materials) standards.<sup>4</sup> In literature, work has been conducted to assess the RF-induced heating for passive implantable medical devices such as stents and orthopedic devices,<sup>17-19</sup> and active implantable medical devices such as deep brain stimulation systems and cardiac pacemakers.<sup>20,21</sup> Most passive devices have a single configuration after implantation and can be evaluated using the standard ASTM procedure,<sup>4</sup> and typical MRI safety test results can be found online at [www.MRIsafety.com](http://www.MRIsafety.com).

Sternal closures are used for the median sternotomy to close the 2 severed or separated sternal halves<sup>22</sup> or to treat the sternal dehiscence.<sup>23,24</sup> Patients with sternal closures generally need to undertake the MRI examination after the implantation to follow up the conditions of human tissues and devices. There are several different sternal closure techniques, such as wire closure,<sup>24,25</sup> band closure,<sup>25</sup> and rigid plate closure.<sup>24,26</sup> For wire closure, it does not have predetermined shapes and dimensions, as the closure needs to be adjusted according to anatomical structures of human bodies. The wire closure can have a simple wire configuration,<sup>27,28</sup> figure-of-8 configuration,<sup>28,29</sup> and Robicsek configuration.<sup>28,30</sup> Among them, the simple wire configuration and figure-of-8 configuration are commonly used standard closure techniques, and the Robicsek configuration and its modifications are often used for patients with high dehiscence risks.<sup>30</sup> A study showed that 776 of 1336

patients needing the sternum closing procedures could have high risk of sternal dehiscence.<sup>31</sup>

Because wire-based sternal closure is usually made of non-ferromagnetic or weak-ferromagnetic materials and no significant heating effects in wire-based sternal closure were documented, it is widely accepted that wire-based sternal closure is not a contraindication for MRI.<sup>32-37</sup> However, the quantitative and accurate analysis of the MRI RF-induced heating for the different sternal closure techniques is still missing. Patients with these implants are usually scanned with low-power protocols due to cautious and conservative considerations, which may limit the flexibility and capability of the imaging procedures. The mechanisms and possible extents of the MRI RF-induced heating for these 3 techniques vary significantly. Therefore, to ensure that patients can be scanned under MRI normally, a thorough study of the RF-induced heating of all wire-closure configurations needs to be performed to explore the intrinsic heating mechanisms and determine the worst-case situations.

In this study, sizes of the wire-based sternal closure were determined based on the anatomically accurate Fats and Billie (girl) models from the virtual population V3.0,<sup>38,39</sup> as these models represent the big and small human body sizes that wire-based sternal closure may be used in. Based on the closure sizes, 3 types of configurations of the large and small wire-based sternal closure with different numbers of closures as well as different spacing for the figure-of-8 configuration were studied in ASTM phantom at 1.5 T and 3 T to determine the possible worst-case heating devices in phantom. With the worst-case heating configurations obtained inside the ASTM phantom, these configurations were simulated in the corresponding human body models (i.e., computational human phantom), to assess the clinically relevant RF-induced heating. To validate the results of these numerical studies, experimental investigations in ASTM phantom were performed. The mechanisms of the RF-induced heating for wire-based sternal closure were further discussed based on the numerical and experimental results. Then, practical advice on the safety of magnetic resonance imaging in patients with wire-based sternal closures was presented for MRI technicians to reference.

## 2 | METHODS

### 2.1 | Device introduction

The commonly used wire-based sternal closure can be classified as 3 main types: simple wire, figure-of-8, and Robicsek.<sup>27-30</sup> Models of these configurations are shown in Figure 1. To meet the need for clinical requirements, various numbers of closures can be used. For the figure-of-8 closures, the spacing between the adjacent closures can also be variable.

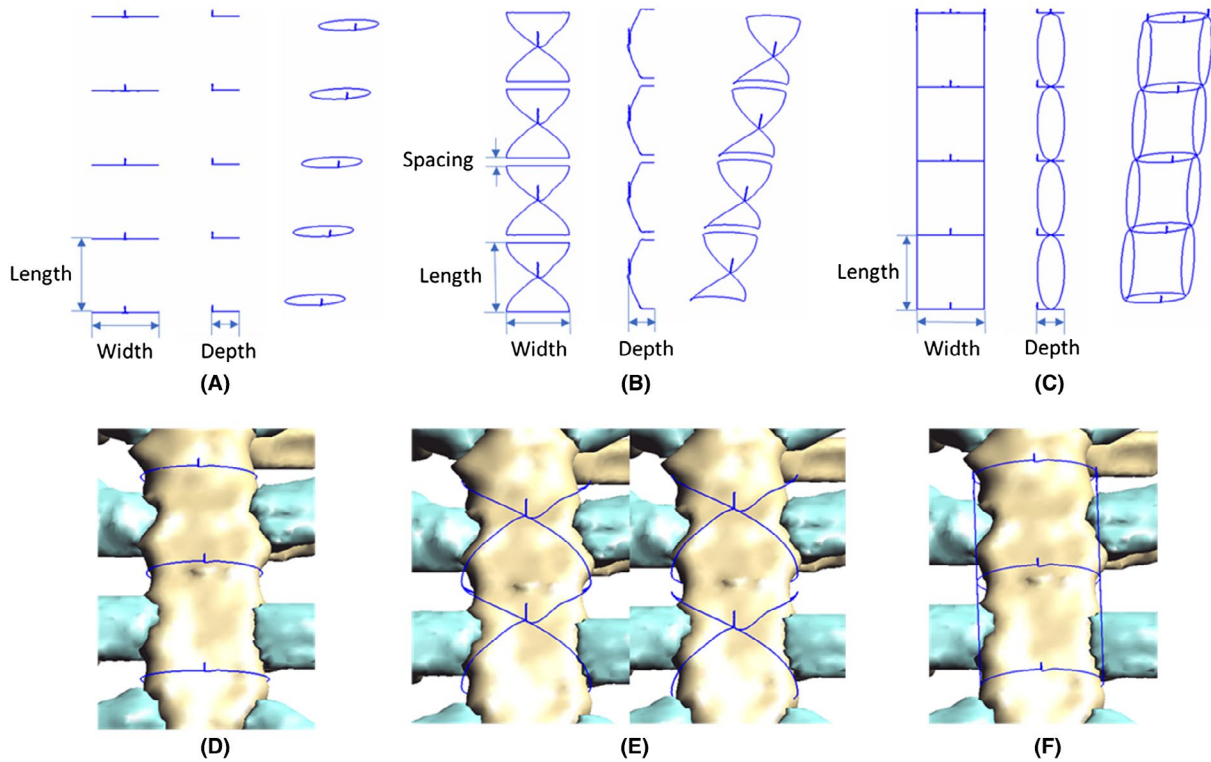


**FIGURE 1** Top: Simulated models: simple wire closure (A), figure-of-8 closure (B), Robicsek closure (C). Bottom: Clinical situations: simple wire closure (D), figure-of-8 closure with touch (left) and without touch (right) (E), and Robicsek closure (F)

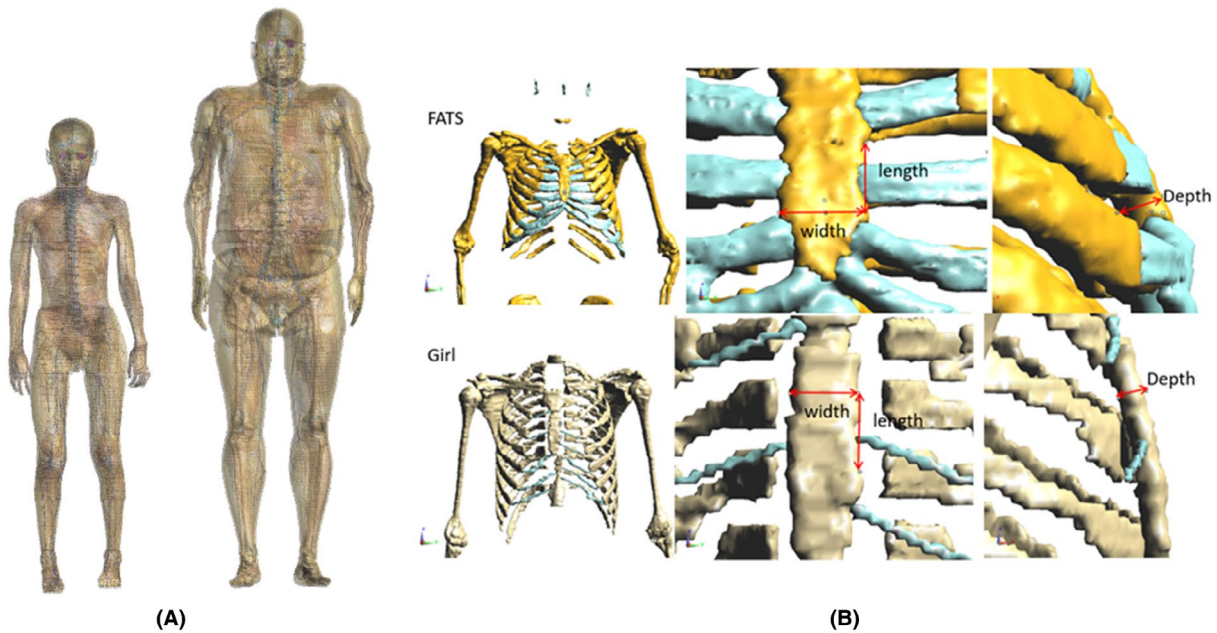


**FIGURE 2** A, Girl model (left) and Fats model (right). B, Measurements for the dimensions

In the study, the dimensions of the simple wire, figure-of-8, and Robicsek closures were determined according to 2 human models: the FATS model and the girl model from the virtual population V3.0,<sup>38,39</sup> as shown in Figure 2. The measured small and large sizes of the wire-based sternal closure were  $20 \times 8.2 \times 21.6$  mm (width  $\times$  depth  $\times$  length) for

the girl (small) model and  $35.2 \times 14.4 \times 30$  mm for the FATS (big) model. To round off the digits, the  $20 \times 8 \times 22$  mm closure was chosen as the small-size closure, while the  $35 \times 14 \times 30$  mm closure was chosen as the large-size closure. The basic parameters of the human models are provided in Table 1.<sup>38,39</sup> Furthermore, the number of closures in the in

**TABLE 1** Basic parameters of the human models<sup>17,18</sup>

Name	Age (years)	Sex	Height (m)	Mass (kg)	Body mass index (kg/m <sup>2</sup> )
Fats	37	Male	1.84	119	35.1
Billie (girl)	11	Female	1.46	36	16.7

in vitro simulations were set as 1 to 5 with increments of 1 for the simple wire closure, and 1 to 4 with increments of 1 for the figure-of-8 and Robicsek closures. For the figure-of-8 closure, the spacing can be 0.5, 2.5, 5.0, 7.5, and 10 mm. Because the sternal wire is very thin (usually about 0.7–0.9 mm) compared with the dimensions of the wire-based sternal closures, the ideal wire model was used to represent the wire to avoid the meshing problem. That meant the thickness of the wire was set to 0 mm in the study.

## 2.2 | Simulations and experiments

### 2.2.1 | Numerical in vitro simulations

Numerical simulations were conducted using the SEMCAD (V14.8 SPEAG) software package based on the finite-difference time-domain method. The RF coils operated at 64 MHz for the 1.5 T system and 128 MHz for the 3 T system. For the in vitro study, the devices were placed inside the ASTM phantom, which was symmetrically loaded in the center of the RF coil.<sup>40</sup> In this study, the coils at 1.5 T and 3 T were high-pass RF transmit body coils, both constructed with 8 parallel rungs, which is a tradeoff between accuracy and complexity. The radius of the coil was 315 mm and the length of the coil was 650 mm. The standard ASTM phantom used in the study was an acrylic container with dielectric constant of 3.7 and electrical conductivity of 0 S/m. The gelled-saline with dielectric constant of 80.4 and conductivity of 0.47 S/m was used to fill the acrylic container. The simulation boundaries enclosing the coil and phantom were all set to be absorbing boundary conditions, and the modes were chosen to be uniaxial perfectly matched layers, which can absorb incoming waves without reflection. The simulation time for each modeling was set to be 25 periods for the RF signals. After the simulations were finished, the currents, voltages, and E/H field signals were examined to guarantee the convergence of all simulations. This modeling has been validated by comparing the strength of the electric field and temperature rises of a reference device at multiple locations inside the phantom from simulations and measurements.

The wire closures are usually made of metallic materials and were set to be PEC (perfect electric conductor) in the simulations. As mentioned previously, the thickness of the wire was set to 0 to avoid the mismatch between the actual wire and the voxelized wire model (which leads to an effective wire thickness around  $0.4 \times$  mesh step). The devices were placed in the ASTM phantom at the middle

in the *y*-direction and *z*-direction and 2 cm away from the longest side wall, as shown in Figure 3, according to the ASTM standard F2182-11a.<sup>40,41</sup> Adaptive meshing was adopted, the maximum mesh step for the sternal closures was set at 0.5 mm, while the maximum mesh steps of the phantom were set at 5 mm and 10 mm. Baselines (enforced meshing reference) were generated on the bounding box of the wire to guarantee the correct distances between the 2 wires. All of the voxelized models were checked to avoid the meshing errors. Once simulations were finished, all the results were normalized to a whole-body specific absorption rate (SAR) of 2 W/kg.

### 2.2.2 | In vitro experiments

In vitro experiments were conducted using the standard ASTM phantom<sup>40,41</sup> for both 1.5 T and 3 T for the validation of in vitro simulations. In the experiments, the temperature rises related to MRI RF-induced heating for the devices were measured and compared against those from simulations. The material of the phantom container is electrically insulated, nonmagnetic, and nonmetallic.<sup>40</sup> The phantom was filled with a gelled saline whose relative permittivity is 80.4 and conductivity is 0.47 S/m,<sup>40</sup> as those in simulations. For the device heating measurement, the temperature probes were placed at the maximum heating location (obtained from simulation result) near the device, as shown in Figure 4. Because the actual absorbed power inside the phantom is not available, the measured temperature rises for a 1/8-in. diameter  $\times$  10-cm-long rod made from titanium were used as a reference to estimate the absorbed power and local incident field in the phantom as follows<sup>41</sup>:

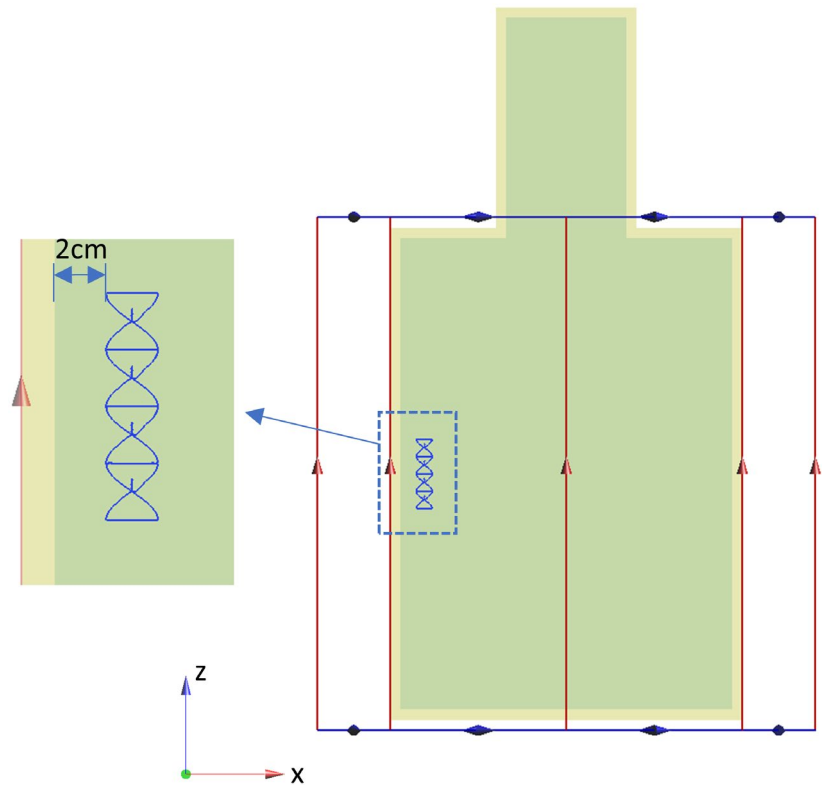
$$T_{\text{meas,wSAR}=2}^d = \frac{T_{\text{meas}}^d}{T_{\text{meas}}^r} T_{\text{simu,wSAR}=2}^r, \quad (1)$$

where  $T_{\text{meas}}^d$  and  $T_{\text{meas}}^r$  are the measured temperature rises of the device under test and the reference rod with the same imaging settings,  $T_{\text{simu,wSAR}=2}^r$  is the simulated temperature rise of the reference rod with a whole phantom-averaged SAR of 2 W/kg, and  $T_{\text{meas,wSAR}=2}^d$  is the calibrated measured temperature rise of the device under test with a whole phantom-averaged SAR of 2 W/kg.

### 2.2.3 | Numerical in vivo simulations

The worst-case heating configurations at 1.5 T and 3 T determined from the in vitro simulations were placed inside

**FIGURE 3** Position of the device in the phantom



the human body models as in Figure 2 to assess the clinically relevant RF-induced heating. The RF coils for 1.5 T and 3 T used in the *in vivo* simulations were the same as those used in the *in vitro* simulations. The human models were placed in 3 different loading positions in the RF coil to present the different imaging regions (Figure 5A). These loading positions would have the closures loaded at the bottom, the center, and the top of the coil. The simulation time was also set to be 25 periods of the RF signals. The wire-based sternal closures were placed in the clinically relevant locations in the human models (Figure 5B,C). Similarly, the mesh sizes for the human body at 1.5 T and 3 T were set at 2 mm, and the maximum mesh steps for the sternal closures were set at 0.5 mm at 1.5 T and 1 mm at 3 T, respectively. All of the results were normalized to a whole-body SAR of 2 W/kg.

### 3 | RESULTS

#### 3.1 | Results of *in vitro* simulations

In the *in vitro* simulations, 8 different closure configurations were investigated. These 8 configurations are the simple wire configurations with large and small loop sizes, Robicsek configurations with large and small loop sizes, and figure-of-8 configurations with small and large loop sizes, and with 0-mm and 5-mm spacing. All 8 configurations were also studied with different number of closures. The results of these in

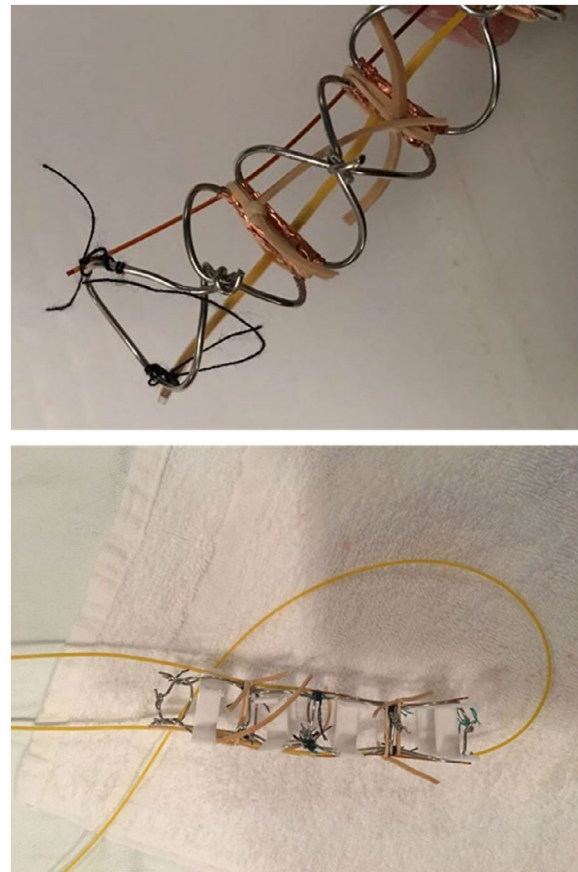


**FIGURE 4** Devices in the experiments and the temperature probes near the devices. Top: 1.5 T; bottom: 3 T

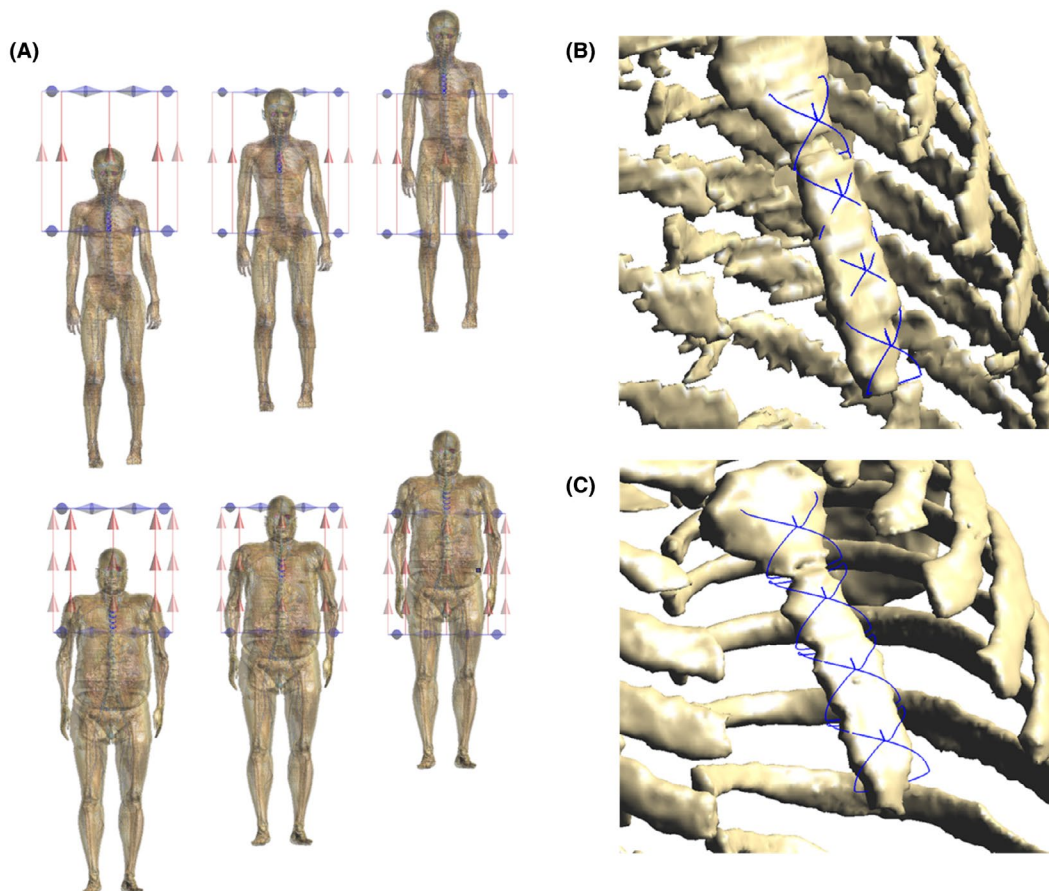


**FIGURE 5** A, Top: Positions of the human model in coil at 1.5 T. The implants were put in the bottom, center, and top of the coil from left to right. Bottom: Positions of the human model in the coil at 3 T. The implants were put in the bottom, center, and top of the coil from left to right. B, Wire closures in human model at 1.5 T. C, Wire closures in human model at 3 T

vitro simulations are shown in Figure 6. Figure 6A shows the peak 1-g averaged specific absorption rate ( $SAR_{1g}$ ) values for different configurations of these sternal closures for both 1.5 T and 3 T. To further investigate the effect of spacing of the figure-of-8 configuration, Figure 6B shows the peak  $SAR_{1g}$  results of the figure-of-8 closure with spacing starting at 0.5 mm internal up to 10 mm.

As shown in Figure 6A, for the 3 closure configurations, the peak  $SAR_{1g}$  of the simple wire closures are much lower than the peak  $SAR_{1g}$  values from other types of closures. For the 2 different closure sizes, the bigger closure configuration generally has the higher peak  $SAR_{1g}$  values than those from the smaller-sized closures at 1.5 T, except for the simple wire configuration. As the number of elements for the closure increases, the peak  $SAR_{1g}$  values of the small-size closures may exceed those from the large-size closures. In addition, the peak  $SAR_{1g}$  will increase as the number of the closures increases in most cases.

For the figure-of-8 closures, to investigate the effect of spacing of the adjacent closures on the RF-induced heating, the number of closures were all set to be 4 and the

simulations were conducted for different spacing of small and big figure-of-8 closures. From the results shown in Figure 6B, the peak  $SAR_{1g}$  will decrease with the increasing of the spacing in most conditions.

From all of these studies, it was determined that the worst-case (highest-peak  $SAR_{1g}$ ) configurations are small figure-of-8 with 4 closures and spacing = 0 at 1.5 T, and big figure-of-8 with 4 closures and spacing = 2.5 mm at 3 T. The SAR distributions of the worst-case configurations at 1.5 T and 3 T are shown in Figure 7. Thermal simulations were conducted for the worse cases under a continuous 15-minute RF exposure for the temperature-rise evaluations. It was determined that the maximum temperature rises for 15 minutes are 9.4°C at 1.5 T and 5.8°C at 3 T.

### 3.2 | Results of experiments

The temperature rise of the worst-case configuration at 1.5 T was measured in the ASTM phantom under continuous 1.5 T MRI RF coil emission for 15 minutes. However, due to the

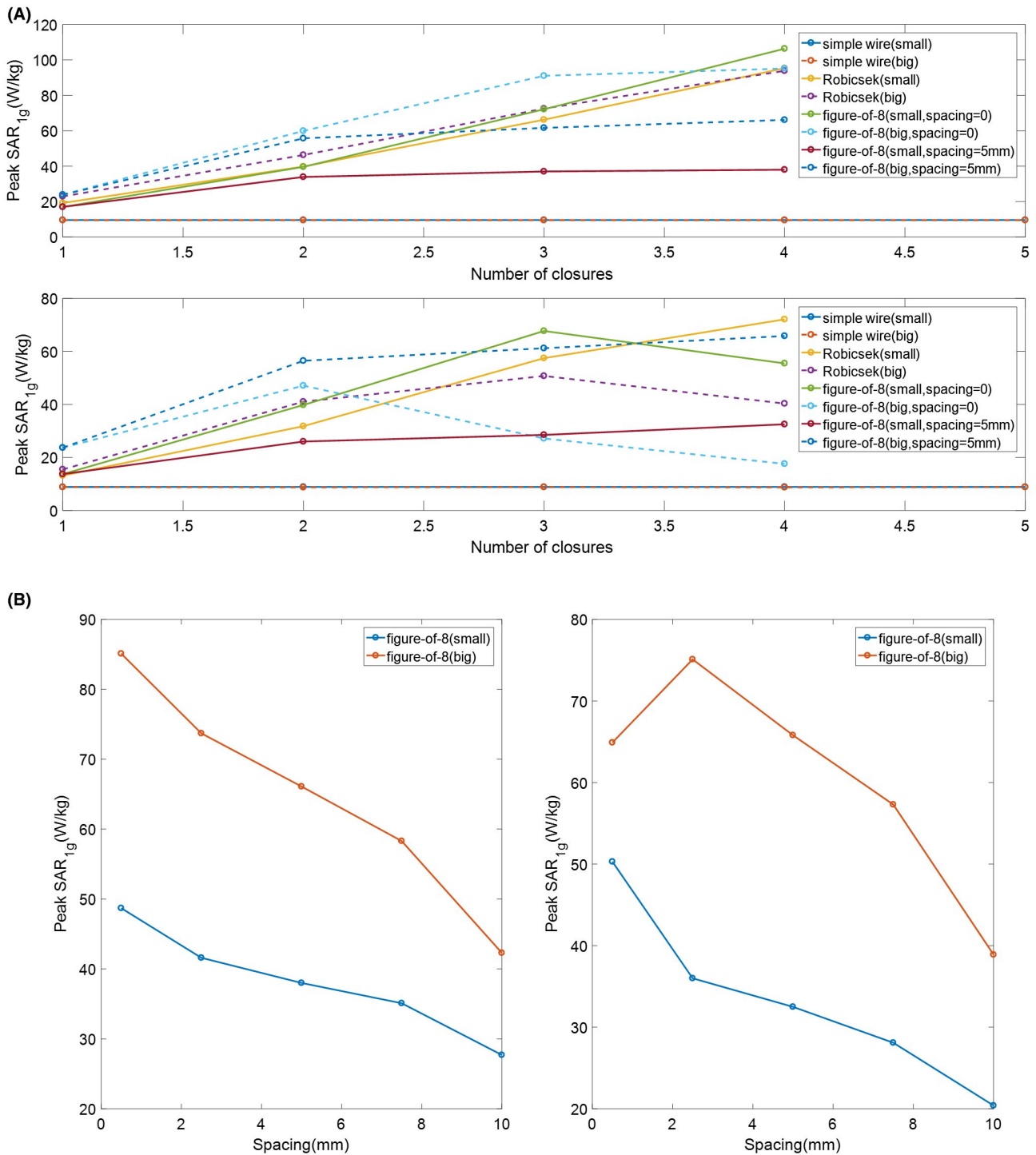


**FIGURE 6** A, Peak 1-g averaged specific absorption rate (SAR<sub>1g</sub>) results of different configurations (simple wire, figure-of-8 with 0-mm and 5 mm-spacing, and Robicsek for 2 sizes) and different number of closures. Top: Results at 1.5 T. Bottom: Results at 3 T. B, Peak SAR<sub>1g</sub> results of the figure-of-8 closures with different spacing. Left: Results at 1.5 T. Right: Results at 3 T

difficulty in constructing the worst-case heating configuration, the construct with the second-highest peak SAR<sub>1g</sub> value was measured for 3 T, which is a small Robicsek with 4 closures. The results of the experiments and corresponding simulations are given in Table 2. All of the results were

normalized to a whole body-averaged SAR value of 2 W/kg. From the results, the temperature rises obtained from the simulations and experiments agree very well with each other under both 1.5 T and 3 T system exposures. This demonstrates the accuracy of the numerical modeling results.

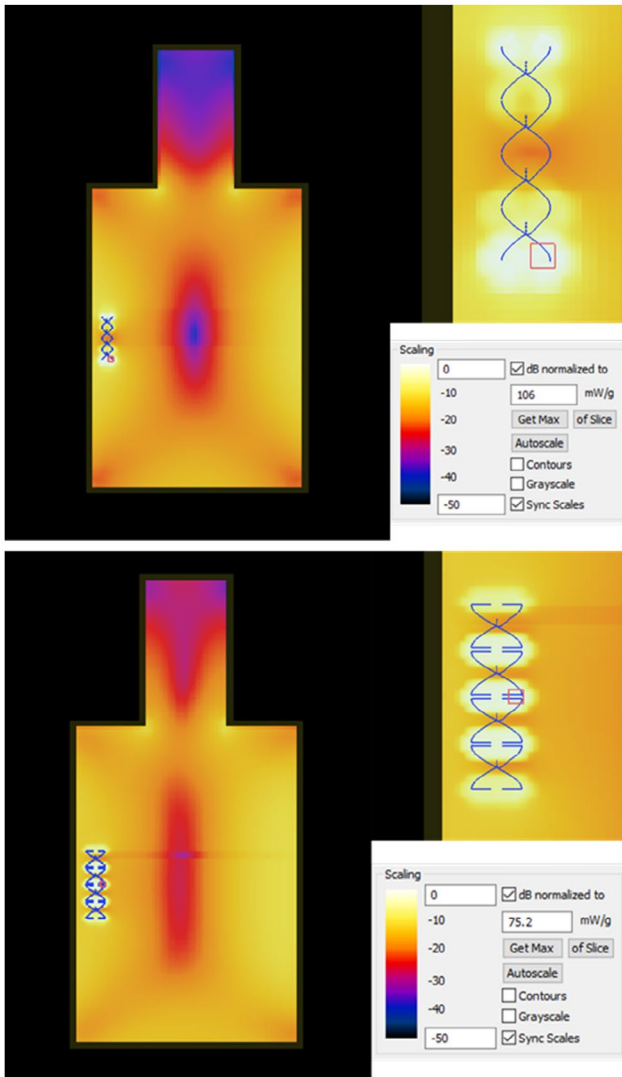


**FIGURE 7** Specific absorption rate distributions of the worst-case configuration in phantom. Top: 1.5 T. Bottom: 3 T

### 3.3 | Results of in vivo simulations

In previous investigations, the devices were placed inside the ASTM phantom for measurement and modeling. ASTM testing/modeling provides an overestimated estimation of the temperature rises. To understand the clinically relevant temperature rises, additional in vivo modeling was performed. As described in the Methods section, the RF-induced heating at 3 different loading positions was investigated. The results of the electromagnetic simulations are shown in Supporting Information Figure S1. The whole body-averaged SAR, overall peak SAR<sub>1g</sub> inside computational human models,

peak SAR<sub>1g</sub> near devices, and the magnitude of B<sub>1</sub> are provided in Table 3. The temperature rises near devices were also calculated using a generic bioheat transfer function thermal model for reference.<sup>42</sup>

As indicated in Table 3, because the sternal closures were placed at the center of the human body models, we observed a significant reduction in peak SAR<sub>1g</sub> values as compared with those from the ASTM phantom modeling. This indicates that the RF-induced heating for clinically relevant scenarios for sternal closures would be lower than those from the ASTM phantom testing, further confirming that the ASTM testing is conservative for this type of implantable devices. In many cases, it was observed that the maximum SAR<sub>1g</sub> values are not near the implanted devices. Therefore, the RF-induced heating under those conditions would not lead to tissue damage.

## 4 | DISCUSSION

Based on the results from in vitro simulations, the simple wire closure always has the lower peak SAR<sub>1g</sub> values as compared with the figure-of-8 and Robicsek closures. Because the element for simple wire closures has no metallic contact to its adjacent element and the adjacent elements are not close to each other, there would be no antenna effect or capacitive coupling (i.e., adjacency) effect, which are the 2 very important factors increasing the RF-induced heating near the device.<sup>18,43,44</sup> The antenna effect refers to the scenario in which the entire device can be considered as a single antenna if the construct electrical length is close to the resonant length. The resonant length is approximately equal to half of the incident signal wavelength, which can be calculated as follows:<sup>43</sup>

$$L_{\text{resonant}} = \frac{\lambda}{2} = \frac{1}{2 \cdot \text{Re}(f \sqrt{\mu \epsilon_c})}, \quad (2)$$

where  $f$  is the operating frequency of MRI (64 MHz for 1.5 T and 128 MHz for 3 T);  $\mu$  is the permeability of the gel and equal to the permeability of the vacuum;  $\epsilon_c$  is the effective permittivity of the gel and  $\epsilon_c = \epsilon - j\sigma/2\pi f$ , in which  $\epsilon$  is the electrical permittivity of the gelled-saline and  $\sigma$  is the conductivity of the gelled saline. Under the ASTM testing condition, the resonant lengths were calculated around 216.2 mm for 1.5 T RF signal and 122.0 mm for 3 T RF signal. As the number of closure elements increases, the peak SAR<sub>1g</sub> will always increase at 1.5 T, because the electrical length of the

**TABLE 2** Temperature rises of the experiments and corresponding simulations

Device	Simulated $\Delta T$ (°C)	Measured $\Delta T$ (°C)	Relative error (%)
Worst case at 1.5 T (small figure-of-8 with 4 closures and spacing = 0)	9.4	7.4	-21.3%
Second worst case at 3 T (small Robicsek with 4 closures)	5.7	5.5	-3.5%

**TABLE 3** Simulated results in human models

	Whole-body SAR (W/kg)	RMS $ B_{1+} $ (Vs/m <sup>2</sup> )	Overall peak SAR <sub>1g</sub> (W/kg)	Peak SAR <sub>1g</sub> near devices (W/kg)	Peak $\Delta T$ near devices (°C)
Device in the bottom of coil at 1.5 T	2	9.65 <sup>6</sup>	74.2	29.9	1.53
Device in the center of coil at 1.5 T	2	5.35 <sup>6</sup>	139.2	32.1	1.64
Device in the top of coil at 1.5 T	2	4.69 <sup>6</sup>	94.3	7.3	0.37
Device in the bottom of coil at 3 T	2	6.91 <sup>6</sup>	84.9	29.2	1.50
Device in the center of coil at 3 T	2	2.72 <sup>6</sup>	62.1	62.1	3.18
Device in the top of coil at 3 T	2	2.02 <sup>6</sup>	49.0	2.3	0.12

configurations will be getting closer to the resonant wavelength. However, the resonant length at 3 T is shorter, and the electrical length of the configurations can be longer than the resonant length at 3 T. Therefore, with the increasing number of closures, the peak SAR<sub>1g</sub> value may increase before the device length reaches resonant length and then decrease after reaching the resonant length.

The capacitive coupling or adjacency effect refers to the interaction effect between adjacent closures that are closely aligned along the longitudinal direction but not connected. The charges near the adjacent ends of the closures are opposite and the spacing is very small; thus, a strong electric field occurs between the 2 ends, which leads to high RF-induced heating. This is similar to a capacitor. Furthermore, the capacitive mutual coupling between the 2 closures can also increase the effective electric length of the devices. If the mutual coupling between the adjacent elements increases, the more RF energy will be stored, which will lead to higher RF-induced heating in the small spacing among elements. Thus, for the figure-of-8 structure, the peak SAR<sub>1g</sub> generally decreases with the increasing of spacing due to such capacitive coupling effect.

The mutual capacitance between the 2 closely spaced wire-based sternal closures is determined primarily by the mutual capacitance between the 2 parallel wires at adjacent ends of the closures, which is<sup>45</sup>:

$$C = \frac{\pi\epsilon l}{\cos^{-1}\left(\frac{d}{2a}\right)}, \quad (3)$$

where  $C$  is the mutual capacitance between the 2 parallel wires;  $d$  is the center-to-center distance between the 2 wires;  $a$  and  $l$  are the radius and length of the wire; and  $\epsilon$  is the electrical permittivity of the gelled-saline. When  $d = 0.5$  mm,  $a = 0.2$  mm, and  $l = 30$  mm, the mutual capacitance  $C = 96.8$  pF; when  $d = 5$  mm,  $a = 0.5$  mm, and  $l = 30$  mm, the mutual capacitance  $C = 29.3$  pF.

The results of the in vitro experiments match those from the in vitro simulations. The mechanisms of the RF-induced heating can be analyzed accurately. In addition, because of the antenna effect and the capacitive mutual coupling effect, the peak SAR<sub>1g</sub> should always locate toward the end of the entire structure or

between the spacing of 2 adjacent closures. This is further illustrated in Figure 7 (in vitro) and in Supporting Information Figure S1 (in vivo). The results of the in vivo simulations also support the heating mechanisms discussed previously.

## 5 | CONCLUSIONS

The in vitro simulations were conducted to determine the possible worst-case heating configurations for wire-based sternal closure under RF exposure for 1.5 T and 3 T systems. Based on the results of these investigations, it was determined that the antenna effect and capacitive mutual coupling effect can be used to explain the configurations' influence on RF-induced heating. In vitro experiments at 1.5 T and 3 T were conducted to validate the in vitro simulation results. The in vivo simulations at 1.5 T and 3 T were used to analyze the SAR distributions of clinically relevant scenarios.

From the study, the peak SAR<sub>1g</sub> of 106.3 W/kg at 1.5 T and 75.2 W/kg at 3 T were observed when the ASTM phantom was used. This leads to temperature rises as high as 9.4°C at 1.5 T and 5.8°C at 3 T. Furthermore, based on the results obtained from the in vivo investigations, the peak SAR<sub>1g</sub> values of 32.1 W/kg at 1.5 T and 62.1 W/kg at 3 T were observed near the devices. Such lower peak SAR<sub>1g</sub> values indicate much lower temperature rises. Therefore, it is possible that patients with sternal closure configurations can be safely scanned under MRI under certain restricted conditions.

The following guidelines can be followed to perform an MRI scan for patients with wire-based sternal closures:

*Non-clinical testing demonstrated that the wire-based sternal closure is MR conditional. A patient with this device can be scanned safely in a MR system immediately after placement under the following conditions:*

- Static magnetic field of 1.5-Tesla and 3 -Tesla, only
- Maximum MR system reported, whole body averaged specific absorption rate (SAR) of 2 W/kg for 15 minutes of

scanning in the Normal Operating Modes of operation for the MR system

- Under the scan conditions defined above, the wire-based sternal closure is expected to produce a maximum temperature rise of 9.4°C after 15-minutes of continuous scanning.

Specifically, the patients with simple wire closures can be scanned without any restrictions, whereas the patients with multiple figure-of-8 and Robicsek closures are generally safe to be scanned in normal operating modes, based on the results of this study. If the total length of the multiple figure-of-8 or Robicsek closures is close to the resonant length (i.e., about 216.2 mm and 122.0 mm at 1.5 T and 3 T), or the adjacent figure-of-8 closures are very close to each other, carefully considerations are needed to ensure that the power is not beyond the normal operating mode. An X-ray scan may be needed to determine the dimensions and locations of the wire-based sternal closures before planning a high-power scan for patients with the closures. External cooling methods, such as using an ice pack, may be useful for the sternal closures usually close to the skin surface. However, the external cooling equipment may also change the RF field near the implants and therefore affect the RF exposure and image quality. Further studies are needed to thoroughly understand the effects of external cooling methods.

## ORCID

Jianfeng Zheng  <https://orcid.org/0000-0001-8998-9561>

Ji Chen  <https://orcid.org/0000-0001-6944-2729>

## REFERENCES

- Aisen AM, Martel W, Braunstein EM, McMillin KI, Phillips WA, Kling TF. MRI and CT evaluation of primary bone and soft-tissue tumors. *Am J Roentgenol*. 1986;146:749–756.
- Dempsey MF, Condon B, Hadley DM. MRI safety review. *Semin Ultrasound CT MR*. 2002;23:392–401.
- Bailey JK, Sammet S, Overocker J, et al. MRI compatibility of silver based wound dressings. *Burns*. 2018;44:1940–1946.
- Woods TO. Standards for medical devices in MRI: present and future. *J Magn Reson Imaging*. 2007;26:1186–1189.
- Sawyer-Glover AM, Shellock FG. Pre-MRI procedure screening: recommendations and safety considerations for biomedical implants and devices. *J Magn Reson Imaging*. 2000;12:92–106.
- Kanal E, Borgstede JP, Barkovich AJ, et al. American College of Radiology White Paper on MR safety. *Am J Roentgenol*. 2002;178:1335–1347.
- Shellock FG, Crues JV. MR safety and the American College of Radiology White Paper. *Am J Roentgenol*. 2002;178:1349–1352.
- Shellock FG, Crues JV. MR procedures: biologic effects, safety, and patient care. *Radiology*. 2004;232:635–652.
- Prasad SK, Pennell DJ. Safety of cardiovascular magnetic resonance in patients with cardiovascular implants and devices. *Heart*. 2004;90:1241–1244.
- Nyenhuis JA, Park S, Kamondetdacha R, Amjad A, Shellock FG, Rezai AR. MRI and implanted medical devices: basic interactions with an emphasis on heating. *IEEE Trans Device Mater Reliab*. 2005;5:467–480.
- Amjad A, Kamondetdacha R, Kildishev AV, Park SM, Nyenhuis JA. Power deposition inside a phantom for testing of MRI heating. *IEEE Trans Magn*. 2005;41:4185–4187.
- Shellock FG. Radiofrequency energy-induced heating during MR procedures: a review. *J Magn Reson Imaging*. 2000;12:30–36.
- Luechinger R, Zeijlemaker VA, Pedersen EM, et al. In vivo heating of pacemaker leads during magnetic resonance imaging. *Eur Heart J*. 2004;26:376–383.
- Gray RW, Bibens WT, Shellock FG. Simple design changes to wires to substantially reduce MRI-induced heating at 1.5 T: implications for implanted leads. *Magn Reson Imaging*. 2005;23:887–891.
- Calcagnini G, Triventi M, Censi F, et al. In vitro investigation of pacemaker lead heating induced by magnetic resonance imaging: role of implant geometry. *J Magn Reson Imaging*. 2008;28:879–886.
- Mattei E, Triventi M, Calcagnini G, et al. Complexity of MRI induced heating on metallic leads: experimental measurements of 374 configurations. *Biomed Eng Online*. 2008;7:11.
- Ji X, Zheng J, Chen J. Numerical evaluation of RF-induced heating for gap and pitch variation of helical stent under MRI. In: *IEEE International Symposium on Antennas and Propagation & USNC/URSI National Radio Science Meeting*. San Diego, CA, 2017;1017–1018.
- Ji X, Zheng J, Yang R, Kainz W, Chen J. Evaluations of the MRI RF-induced heating for helical stents under a 1.5 T MRI system. *IEEE Trans Electromagn Compat*. 2019;61:57–64.
- Li D, Ji X, Zheng J, Pan C, Chen J, Kainz W. A novel design of implantable esophageal stent to reduce the MRI RF-induced heating. *IEEE Trans Electromagn Compat*. 2017;59:805–812.
- Baker KB, Tkach JA, Phillips MD, Rezai AR. Variability in RF-induced heating of a deep brain stimulation implant across MR systems. *J Magn Reson Imaging*. 2006;24:1236–1242.
- Gorny KR, Presti MF, Goerss SJ, et al. Measurements of RF heating during 3.0-T MRI of a pig implanted with deep brain stimulator. *Magn Reson Imaging*. 2013;31:783–788.
- Shifrin EG, Nickelshpur GS, Shvartsman MD, Umansky MA. *Sternal Closure System, Method and Apparatus Therefore*. US Patent 7,651,498[P]. January 26, 2010.
- Taber RE, Madaras J. Prevention of sternotomy wound disruptions by use of figure-of-eight pericostal sutures. *Ann Thorac Surg*. 1969;8:367–369.
- Pai S, Gunja NJ, Dupak EL, et al. In vitro comparison of wire and plate fixation for midline sternotomies. *Ann Thorac Surg*. 2005;80:962–968.
- Orhan SN, Ozyazicioglu MH, Colak A. A biomechanical study of 4 different sternum closure techniques under different deformation modes. *Interact Cardiovasc Thorac Surg*. 2017;25:750–756.
- Ozaki W, Buchman SR, Iannetoni MD, Frankenburg EP. Biomechanical study of sternal closure using rigid fixation techniques in human cadavers. *Ann Thorac Surg*. 1998;65:1660–1665.
- Losanoff JE, Basson MD, Gruber SA, Huff H, Hsieh F. Single wire versus double wire loops for median sternotomy closure:

- experimental biomechanical study using a human cadaveric model. *Ann Thorac Surg.* 2007;84:1288–1293.
28. Losanoff JE, Collier AD, Wagner-Mann CC, et al. Biomechanical comparison of median sternotomy closures. *Ann Thorac Surg.* 2004;77:203–209.
  29. Murray KD, Pasque MK. Routine sternal closure using six overlapping figure-of-8 wires. *Ann Thorac Surg.* 1997;64:1852–1854.
  30. Tavilla G, van Son JA, Verhagen AF, Lacquet LK. Modified Robicsek technique for complicated sternal closure. *Ann Thorac Surg.* 1991;52:1179–1180.
  31. Sharma R, Puri D, Panigrahi BP, Viridi IS. A modified parasternal wire technique for prevention and treatment of sternal dehiscence. *Ann Thorac Surg.* 2004;77:210–213.
  32. Manner I, Alanen A, Komu M, Savunen T, Kantonen I, Ekfors T. MR imaging in the presence of small circular metallic implants: assessment of thermal injuries. *Acta Radiol.* 1996;37:551–554.
  33. Hartnell GG, Spence L, Hughes LA, Cohen MC, Saouaf R, Buff B. Safety of MR imaging in patients who have retained metallic materials after cardiac surgery. *AJR Am J Roentgenol.* 1997;168:1157–1159.
  34. Shellock FG. *Reference Manual for Magnetic Resonance Safety.* Philadelphia, PA: WB Saunders; 2002:728–729.
  35. Prasad SK, Pennell DJ. Safety of cardiovascular magnetic resonance in patients with cardiovascular implants and devices. *Heart.* 2004;90:1241–1244.
  36. Levine GN, Gomes AS, Arai AE, et al. Safety of magnetic resonance imaging in patients with cardiovascular devices. *Circulation.* 2007;116:2878–2891.
  37. Baikoussis NG, Apostolakis E, Papakonstantinou NA, Sarantitis I, Dougenis D. Safety of magnetic resonance imaging in patients with implanted cardiac prostheses and metallic cardiovascular electronic devices. *Ann Thorac Surg.* 2011;91:2006–2011.
  38. Neufeld E, Gosselin M, Murbach M, Christ A, Cabot E, Kuster N. Analysis of the local worst-case SAR exposure caused by an MRI multi-transmit body coil in anatomical models of the human body. *Phys Med Biol.* 2011;56:4649.
  39. Christ A, Kainz W, Hahn EG, et al. The virtual family—development of surface-based anatomical models of two adults and two children for dosimetric simulations. *Phys Med Biol.* 2009;55:N23.
  40. Liu Y, Chen J, Shellock FG, Kainz W. Computational and experimental studies of an orthopedic implant: MRI-related heating at 1.5-T/64-MHz and 3-T/128-MHz. *J Magn Reson Imaging.* 2013;37:491–497.
  41. ASTM. *Standard F2182-11a. Standard Test Method for Measurement of Radio Frequency Induced Heating on or Near Passive Implants During Magnetic Resonance Imaging.* West Conshohocken, PA: ASTM International; 2011.
  42. Shrivastava D, Vaughan JT. A generic bioheat transfer thermal model for a perfused tissue. *J Biomech Eng.* 2009;131:074506.
  43. Dempsey MF, Condon B, Hadley DM. Investigation of the factors responsible for burns during MRI. *J Magn Reson Imaging.* 2001;13:627–631.
  44. Guo R, Zheng J, Wang YU, et al. Computational and experimental investigation of RF-induced heating for multiple orthopedic implants. *Magn Reson Med.* 2019;82:1848–1858.
  45. Pozar DM. *Microwave Engineering.* New York: John Wiley & Sons; 2012.

## SUPPORTING INFORMATION

Additional supporting information may be found online in the Supporting Information section at the end of the article.

**FIGURE S1** Top: the SAR distributions at 1.5 T in human model: left: the device was in the bottom of the coil; center: the device was in the center of the coil; right: the device was in the top of the coil. Bottom: the SAR distributions at 3 T in human model: left: the device was in the bottom of the coil; center: the device was in the center of the coil; right: the device was in the top of the coil

**How to cite this article:** Zheng J, Xia M, Kainz W, Chen J. Wire-based sternal closure: MRI-related heating at 1.5 T/64 MHz and 3 T/128 MHz based on simulation and experimental phantom study. *Magn Reson Med.* 2020;83:1055–1065. <https://doi.org/10.1002/mrm.27963>